Energy 239 (2022) 122405

Contents lists available at ScienceDirect

Energy

journal homepage: www.elsevier.com/locate/energy

Design and modeling of a honeycomb ceramic thermal energy storage for a solar thermal air-Brayton cycle system

Xin Zhou [1], Haoran Xu [1], Duo Xiang, Jinli Chen, Gang Xiao *

State Key Laboratory of Clean Energy Utilization, Zhejiang University, Hangzhou, China

ARTICLE INFO

Article history:
Received 31 May 2021
Received in revised form
5 October 2021
Accepted 20 October 2021
Available online 22 October 2021

Keywords:
Solar thermal air-Brayton cycle
Thermal energy storage
Honeycomb ceramics
Mathematical modeling

ABSTRACT

Solar thermal air-Brayton cycle system stands out among distributed power systems with high reliability, compactness, low cost and little water consumption, but its operation is affected by the availability and stability of solar energy. Thermal energy storage (TES) is necessary for dispatchable power generation and stable operation of solar thermal air-Brayton systems, but there are insufficient studies on the integrated TES-solar air-Brayton cycle system. In this paper, a honeycomb ceramic TES was designed for a 10 kW-scale solar air-Brayton cycle system based on the steady state off-design cycle analysis. The TES presented high efficiencies in the charging and discharging experimental tests, which were 79.6% and 76.5%, respectively. The air leakage between the ceramic modules was founded to affect the outlet air temperature and module temperature. Besides, a one-dimensional transient TES model was developed and validated. A feasible stand-alone operation strategy for the system was finally simulated based on the transient system model, which showed that constant output electric power (~12 kW) and extended power generation duration of 3 h could be realized by integrating the TES. This work contributes to the design and modeling of TES for solar air-Brayton cycle systems as well as the system operation strategy analysis.

1. Introduction

Solar thermal open Brayton cycle is an advanced power system because of its high reliability, stable operation, little water consumption and low cost [1–3]. Since the last decade, a number of projects on solar air-Brayton cycle system were implemented. From 2010 to 2014, CSIRO and Mitsubishi Heavy Industries (MHI) established a 200 kWe solar-tower air-Brayton cycle system with a 600 kW_{th} tubular air receiver achieving an outlet temperature at 1123 K [4]. Dickey et al. also tested a solar air-Brayton cycle power system with an output electric power of 25 kW and a system efficiency of 13.8% on the Weizmann Institute solar tower in 2011 [5]. The EU-funded OMSoP (Optimised Microturbine Solar Power system) project in 2013–2017 further demonstrated a solar dish-micro turbine power system, which had a nominal output electric power of 5–10 kWe and a volumetric receiver with the thermal efficiency of 82% at 1073 K [6,7].

Thermal energy storage (TES) is vital for the dispatchability of these solar thermal air-Brayton cycle systems, because TES can extend power generation duration by transferring excessive solar energy to the period without solar radiation, thus ensuring its continuous operation and improving the utilization efficiency of solar energy. Besides, the integration of TES can alleviate the influence of unstable solar radiation on the fluctuation of turbine temperature [8,9] and shorten the warm-up period [10]. To enhance the heat transfer process with a large heat transfer area and a compact structure, a TES in packed-bed configuration of solid storage materials is usually adopted. Honeycomb ceramic storage is a promising option because it has a large specific surface, small pressure drops of straight channels and a good thermal shock resistance [11–13].

In 2009, DLR investigated a honeycomb ceramic storage system with four parallel chambers filled with honeycomb ceramic modules [14]. The system had a storage capacity of 9 MWh and a total volume of 120 m^3 and showed an excellent performance in the charging-discharging cycling tests between 393 K and 953 K. In 2013, DLR further investigated the packed-bed sensible heat storage systems with three kinds of materials in the HOTSPOT project, including a broken basalt, a ceramic sphere and a ceramic honeycomb, among which the honeycomb ceramic stands out in thermal

* Corresponding author.
E-mail address: xiaogangtianmen@zju.edu.cn (G. Xiao).

[1] These authors contributed equally to this paper.

https://doi.org/10.1016/j.energy.2021.122405
0360-5442/

Nomenclature

A	area (m^2)
C_p	specific heat capacity at constant pressure ($J \cdot kg^{-1} \cdot K^{-1}$)
C_v	specific heat capacity at constant volume ($J \cdot m^{-3} \cdot K^{-1}$)
DNI	direct normal irradiance ($W \cdot m^{-2}$)
f	fanning friction factor
h	heat transfer coefficient ($W \cdot m^{-2}$)
L	flow channel length (m)
$\dot{m}$	mass flow rate ($kg \cdot s^{-1}$)
M_{st}	total mass of storage medium (kg)
N	rotation speed (krpm)
p	pressure (kPa)
$\dot{P}_e$	output electric power (kW)
$\dot{q}$	thermal power (W or kW)
Q	thermal energy (MJ)
Re	Reynolds number
SM	surge margin
T	temperature (K)

Greek symbols

α	leakage ratio
η	efficiency
γ	adiabatic exponent of air
ρ	density ($kg \cdot m^{-3}$)
μ	dynamic viscosity ($Pa \cdot s$)
π	pressure/expansion ratio
ε	effectiveness of recuperator
λ	thermal conductivity ($W \cdot m^{-1} \cdot K^{-1}$)
σ	porosity of the module
Δp	pressure drop (kPa)

Subscripts

a	ambient
c	compressor; cold flow channel of recuperator
ch	charging process
d	design point
dis	discharging process
e	electricity
f/g	fluid
h	hot flow channel of recuperator
o	stagnation state
rec	receiver
s	isentropic process; solid
t	turbine

Abbreviations

CSIRO	Commonwealth Scientific and Industrial Research Organisation
DLR	Deutsches Zentrum für Luft-und Raumfahrt
OMSoP	Optimised Microturbine Solar Power system
SolGATS	Concentrated Solar Power micro gas turbine with thermal energy storage
TES	thermal energy storage
TOT	turbine outlet temperature
TIT	turbine inlet temperature

utilization efficiency [15]. In their tests, the maximum charging temperature reached 1103 K and the nominal discharged heat rate was about 11 MW_{th}. They also proposed designs of the packed-bed TES to uniform the inlet flow distribution and reduce the pressure loss and the thermal-mechanical force. Wang et al. [12] experimentally investigated the charging-discharging performance of a packed-bed TES filled with 4000 pieces of ceramic honeycombs between 303 K and 923 K with atmospheric air as the heat transfer medium. They found the charging/discharging rate was related to temperature difference and air flow rate. Mahmood et al. [9,16] tested the thermal performance of a cylindrical TES tank stacked with 5 pieces of ceramic honeycombs under 723 K and the pressure drop was around 1.1% with respect to inlet air pressure. Luo et al. [17] tested a small honeycomb ceramic TES consisting of 4 pieces of cubic module. Their results showed the TES had a charging-discharging cyclic efficiency of 66%. These laboratory/pilot scale tests have proved the feasibility of the honeycomb ceramic as high-temperature storage materials.

Mathematical model of honeycomb ceramic TES is useful for analyzing its thermal performance in the charging-discharging process. Schmidt et al. [18] presented a transient model of a solid thermal storage unit with rectangular cross-sectional channels based on the one-dimensional energy conservation equation of fluid and the two-dimensional heat conduction equation of solid, where heat conduction in both the axial and the radial directions were considered. Andreozzi et al. [19] solved three-dimensional differential governing equations of mass, momentum and energy for the heat transfer process in a high-temperature cordierite-based honeycomb TES with air as the working fluid. To simplify the TES simulation, one-dimensional models formed by volume-averaged energy conservation equations were studied by Luo et al. [17] and Li et al. [20], where the solid heat conduction in transverse direction was neglected with thin wall assumption. Mahmood et al. [16] considered all the channels of honeycomb ceramic TES in their one-dimensional model based on the energy conservation equations. These models were validated by experimental results of small thermal storage device with atmospheric air as the heat transfer fluid.

For solar thermal Brayton cycle power system with solar energy as the only heat source, its operation stability and duration would be greatly affected by solar radiation condition. However, there has been rare studies about the integration of thermal energy storage into pure-solar thermal Brayton cycle power systems, which calls for research on the design and experimental tests of low-cost TES specifically for those systems. Besides, it's necessary to conduct performance analysis of the system integrated with TES for the development of the operation and control strategies. Compared with two- and three-dimensional modeling methods, one-dimensional modeling of TES is more suitable for system simulation because of its simplicity and less computational effort. Existing one-dimensional numerical studies on honeycomb ceramic TES consider ideal flow conditions inside the device, which is not applicable for a large TES tank with many stacked modules, and the TES model should be specially modified based on experimental results. In this study, design, test and modeling of a honeycomb ceramics packed-bed thermal storage tank for a solar air-Brayton cycle power system are conducted to achieve a required thermal energy storage capacity for the continuous operation of the system when there is no solar radiation. The design for TES with high-temperature pressurized air as the heat transfer fluid is experimentally studied and a one-dimensional transient model of the designed large thermal storage tank is developed by taking the air leakage into consideration. Lastly, a transient system model during a typical day is established to verify its feasibility. All the mathematical models are developed in the MATLAB environment.

2. System configuration

As shown in Fig. 1a, the system studied in this paper consists of a micro gas turbine (including a centrifugal compressor, a radial turbine and a generator connected in one spool), a recuperator, an air receiver and a thermal storage tank. A small heliostat field provides concentrated solar power for the system.

The system has three operation modes, i.e., the receiver-only mode, the storage-charging mode and the storage-discharging mode. In the receiver-only mode, the compressed air will be heated by the receiver (with the on/off valve in off-state) and the thermal storage doesn't work (with the control valve open). In the storage-charging mode, partial high-temperature air after the receiver will flow through the storage tank by adjusting the control valve. When there is no solar energy input, the system will work in the storage-discharging mode and the storage tank will release heat to the air for power generation (with the control valve closed and the on/off valve in on-state).

2.1. Design parameters

The main design parameters are specified in Table 1. Component efficiencies and pressure drop coefficients are assumed at the initial design process based on the existing research. Maximum turbine inlet temperature is 1073 K and maximum turbine outlet temperature is 923 K, which are limited by the material properties of turbine and recuperator, respectively.

When operating at the storage-charging mode, the system input energy is the incident radiation power at the receiver aperture $\dot{q}_{solar}$ and the power generation efficiency η_e can be defined as shown in Eq. (1).

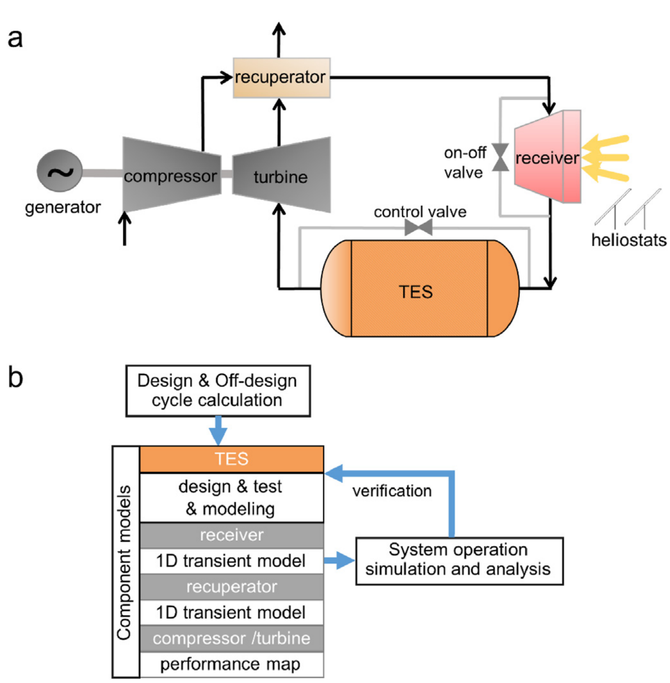

Fig. 1. (a) System configuration and (b) Flow chart of research method.

$$\eta_e = \frac{P_e}{\dot{q}_{solar}} \tag{1}$$

When operating at the storage-discharging mode, the thermal power absorbed by air flowing through the storage tank is denoted as $\dot{q}_f$, and the power generation efficiency η_e can be defines shown in Eq. (2).

$$\eta_e = \frac{P_e}{\dot{q}_f} \tag{2}$$

The design requirements for the thermal energy storage in this system include: (a) average output electric power $\overline{P}_e > 5$ kW during the operation period; (b) thermal storage capacity for 3-h system operation during its discharging period. Therefore, the total amount of discharged thermal energy during the discharging period is initially estimated as shown in Eq. (3), where the average output electric power $\overline{P}_e$ and the power generation efficiency $\overline{\eta}_e$ are initially assumed to be 5 kW and 15%, respectively. Besides, due to the heat loss of the storage tank, its thermal efficiency $\eta_{storage}$ is assumed to be 70% according to literature [17,25].

$$Q_{storage} = \frac{\overline{P}_e \cdot t}{\overline{\eta}_e \eta_{storage}} = \frac{5kW \times 3h \times 3.6}{0.15 \times 0.7} = 514.3MJ \tag{3}$$

2.2. Analysis flowchart

The analysis process for the design of the TES is illustrated in Fig. 1b. Firstly, steady state off-design calculation of the system is performed to determine the temperature drop of storage medium during the discharging period, based on which the total mass of storage medium can be determined. Then the experimental tests of the TES are carried out and related mathematical models will be developed. Lastly, the transient system models, including the sub-models of the centrifugal compressor, the radial turbine, the recuperator and the air receiver are developed to simulate the system performance during a typical day. In this way, the feasibility of the TES can be verified.

3. Off-design analysis of system

The total mass of storage medium M_{st} is determined by the discharged thermal energy $Q_{storage}$ and the temperature drop of the storage medium during the discharging period as shown in Eq. (4).

$$Q_{storage} = M_{st} \int_{T_{df}}^{T_o} c_p dT \tag{4}$$

Here T_o and T_{df} are the initial and the final temperatures of the storage medium in the discharging process, respectively. T_o depends on the charging process and the maximum value is 1073 K when the storage is fully charged.

In the discharging mode, with heat transferring from the storage tank to the air, the output electric power gradually decreases with the decline of the storage outlet temperature. As there is no net output power when turbine inlet temperature TIT is below the minimum value TIT_{min}, the lowest outlet temperature of the storage tank at the end of discharging period is considered to be TIT_{min}, which is also the final temperature of the storage medium T_{df}. In this paper, the storage tank is assumed to be fully discharged and the system will stop running when the output electric power

Table 1
Design parameters of the system.

Design parameter		Value	Unit
rotation speed N_d		120	krpm
mass flow rate $\dot{m}$		0.16	kg/s
Compressor	pressure ratio π_c	3	–
	adiabatic efficiency η_c[21]	75	%
Turbine	expansion ratio π_t	2.8	–
	adiabatic efficiency η_t[22]	80	%
Recuperator	effectiveness ε[23]	0.85	–
	pressure drop coefficient $\Delta p/p_{in}$	2	%
Air receiver	thermal efficiency η_{rec}[24]	65	%
	pressure drop coefficient $\Delta p_{rec}/p_2$	2	%
	absorbed thermal power $\dot{q}_u$	47.48	kW
	incident solar power $\dot{q}_{solar}$	73.05	kW
Storage tank	pressure drop coefficient $\Delta p_{storage}/p_2$	1.5	%
mechanical efficiency η_{mec}		0.95	–
generator efficiency η_g		0.9	–
output electric power P_e		10.974	kW
power generation efficiency η_e		15.02	%

is < 0.5 kW. Therefore, off-design calculation of the system (without TES) is performed to determine the final temperature of storage medium during the discharging period for the TES.

The input thermal power for the system is assumed to be proportional to*DNI* with a constant efficiency of the heliostat field and an intercept factor of receiver. Fig. 2a shows the calculation flow chart of working points with constant *TIT* operation for the system, which is based on the balance principles of mass, pressure and rotation speed of the Brayton cycle.

Working points of the compressor at the constant *TIT* are presented in Fig. 2b. For each rotation speed, a higher *TIT* means a working point closer to the surge line, especially at the low rotation speed (84 krpm–96 krpm). Therefore, it's necessary to ensure that the compressor surge margin is above 10% when the system runs at a low speed [26,27]. As can be seen in Fig. 2c, when *TIT* is equal to 653 K, the output electric power is < 0.5 kW with the rotation speed within 85.8krpm–93.6krpm. Therefore, T_{df} is determined to be 653 K, which is also the final temperature of the storage tank at the end of discharging period.

4. TES for the system

4.1. TES design

A mullite-based honeycomb ceramic was used as the unit TES module as shown in Fig. B.1 (Appendix B). The physical properties of the mullite-based ceramic are shown in Table 2. The thermal conductivity and the specific heat capacity are derived from the study of Guan et al. [28].

Given the initial temperature T_o (1073 K) and final temperature

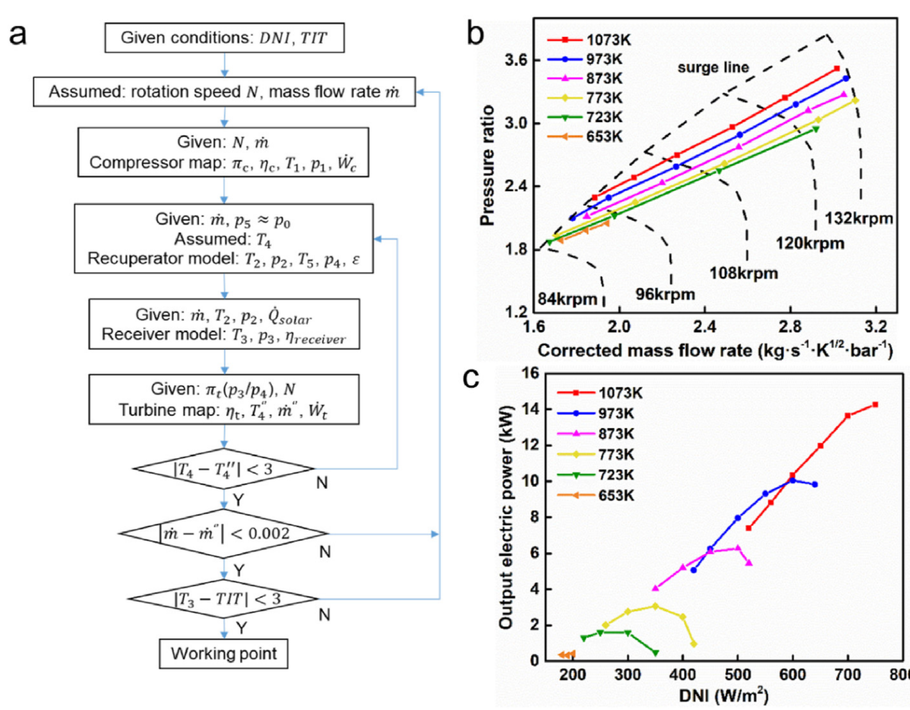

Fig. 2. Off-design analysis at constant TIT operation: (a) flow chart of the cycle calculation, (b) compressor working points shown on its performance map, and (c) output electric power of the system.

Table 2
Properties of the mullite-based ceramic.

Property	Value	Temperature range
True density ($kg \cdot m^{-3}$)	$\rho_s = 1920$	–
Thermal conductivity ($W \cdot m^{-1} \cdot K^{-1}$)	$\lambda_s = -1.21156 \cdot 10^{-9} T^3 + 5.89207 \cdot 10^{-6} T^2 - 0.00922T + 8.75599$	300–1420 K
Specific heat capacity ($J \cdot mol^{-1} \cdot K^{-1}$)	$C_s = -111.52 \cdot 10^5 T^{-2} + 0.06253T + 365.96$	298–1100 K

T_{df} (653 K) of the storage modules during the discharging period, the total mass of ceramic modules M_{st} can be calculated as shown in Eq. (5).

$$M_{st} = \frac{Q_{storage}}{\int_{T_{df}}^{T_0} c_p dT} \approx 1291.3kg \tag{5}$$

It is assumed that the flow inside the stacked modules is the laminar flow in parallel straight channels [17,20], so that the structure size of the stacked modules can be calculated by Eqs. (6) and (7).

$$A_g = \frac{\dot{m}}{\rho_g \cdot u_m} = \sigma \cdot A_{sf} = \sigma \cdot L_{sf}^2 \tag{6}$$

$$L = \frac{M_{st}}{\rho_s \cdot A_{sf} \cdot (1-\sigma)} \tag{7}$$

Here u_m is the air velocity inside the stacked modules, A_g is the total flow cross section area, A_{sf} is the total cross section area, L_{sf} is the side length of cross section, σ is porosity of the module, and L is the total length of the stacked modules. According to the design condition, the mass flow rate $\dot{m}$ inside the storage tank is 0.16 kg/s and the air density ρ_g is approximately equal to that at the storage inlet. The pressure drops of stacked modules Δp are estimated by Eq. (8) – (10).

$$\Delta p = \left(\frac{4fL}{d_h} + \sum K \right) \cdot \frac{\rho_g \cdot {u_m}^2}{2} \tag{8}$$

$$f = \frac{16}{Re} \tag{9}$$

$$Re = \frac{\rho_g \cdot u_m \cdot d_h}{\mu} \tag{10}$$

Here f is the fanning friction factor for laminar flow, Re is the Reynolds number, d_h is the hydraulic diameter of flow channels, and $\sum K$ is the sum of local flow resistance coefficients. The design of the stacked modules is developed in MathCAD by iterating Eqs. (5)–(10) with the air velocity ranging from 0.3 to 5 m/s [29,30]. Considering the space limitation of the test site, main constraints of the design are $\Delta p / p_{in} \leq 1.5\%$ and $L \leq 1.6$m.

The final layout of the stacked modules contains 16 layers with 49 blocks in each layer as presented in Fig. 3a. The total mass is reduced to 835 kg due to the space limitation of the storage tank. As further illustrated in Fig. 3b and c, with the compressed air as the heat transfer fluid, the storage tank was designed in cylinder shape with a total outer diameter of 1.53 m for pressure-bearing. To prevent the air from flowing out of the stacked modules, the space between the square-section stacked modules and the cylinder shell is filled with alumina-silicate fiber felt. However, there still exists some space that couldn't be completely filled. The tank was well insulated by insulation castables (inner layer) and the alumina-silicate fiber felt (outer layer), and the modules were supported by the refractory castables from the bottom of the tank. Due to the large difference between the cross-sectional area of the connecting pipe and the tank, several metal deflector plates were arranged at the front of the stacked modules to distribute the air flow evenly on the cross section of the modules. There were also deflector plates to collect the air flow at the back of the stacked modules. The whole storage tank was horizontally placed, where a main hole was open at the middle of the storage tank for the placement of modules. Three thermocouples are arranged at the left, middle and right positions on each module layer to measure the module temperature as shown in Fig. 3 (d) and (e)., where T_0 and T_{16} are the inlet air temperature and outlet air temperature of the stacked modules. The thermocouple probes are in contact with the module surface.

4.2. Experimental tests

The test rig of the storage tank is presented in Fig. 4. During the charging process, compressed air was provided by the screw compressor and heated by the air receiver before entering and heating the storage tank. Residual heat of the air was recovered in the recuperator for preheat purposes. During the discharging process, the compressed air went through the same route and absorbed heat from the storage tank. Measurement parameters include T_0~T_{16}, air pressures at the inlet/outlet of the TES and air flow rate. Table 3 shows the measurement instruments used in the tests.

Two tests were conducted based on the test rig, of which the temperature changes with the operating time are shown in Fig. 5. The first test started from 11:10 to 19:56 on a sunny day, during which the charging and discharging periods were from 11:10 to 17:00 (0–21,000 s) and 17:00 to 19:56 (21,000–31,560 s), respectively. As shown in Fig. 5a, mass flow rate during the first test was kept around 0.077 kg/s with small fluctuation and the pressure drop was almost between 4.3 kPa and 4.8 kPa. The second test was conducted on the second day, where the charging and discharging period lasted for 23,000 s and 6300 s, respectively. As seen in Fig. 5c, the storage tank was charged with different mass flow rate during the second test and the pressure drop changed obviously with the mass flow rate.

As shown in Fig. 5b, the maximum inlet temperature of the stacked modules T_0 reached 1076 K within 7000 s and then fluctuated, while the outlet air temperature T_{16} continuously rose in the whole charging period and reached 807 K at 21,000 s. In the discharging period, T_0 declined rapidly from 944 K to 610 K within 1 h (21,000–24,600 s), while a slight increase of T_{16} from 807 K to 816 K was observed before slowly decreasing to 704 K at the end of the test. The temperature evolutions on different module layers are further presented in Fig. 5b. The temperature of front layers (3rd and 6th) showed a similar variation trend with the inlet air temperature, while no fluctuation was observed in the latter layers (9th and 13th). The peak temperature of the 3rd layer reached 1066K at 8568s, while the temperature of the 13th layer was continuously growing in the charging period and only reached 851 K at the end of charging (21,000 s). In the discharging period, the temperature of front layers decreased quickly, while the latter layers showed an increase for a period before their gradual decline. This was mainly because the heat stored in the front layers was transferred to the

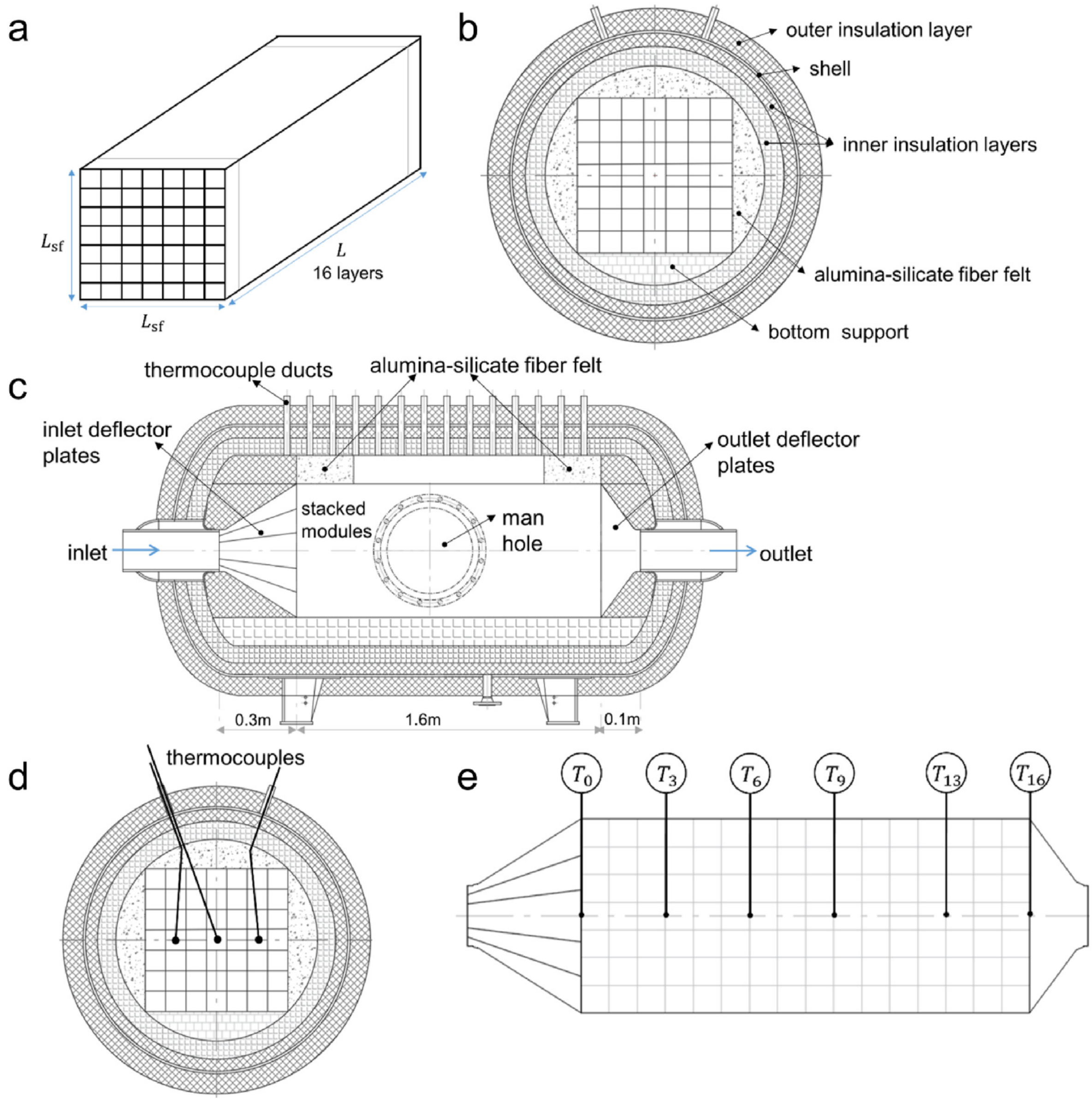

Fig. 3. Schematic of the (a) stacked modules, (b) cross section of the storage tank, (c) vertical section of the storage tank, (d) layout of thermocouples in cross section and (e) vertical section.

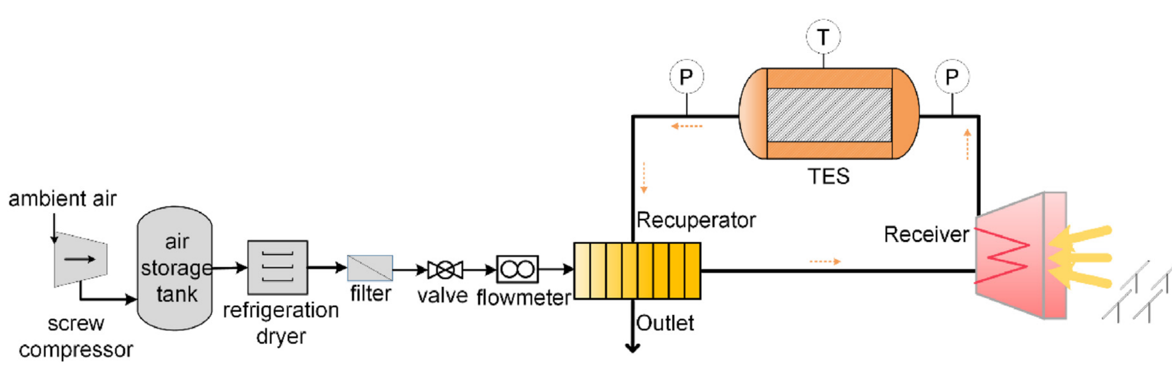

Fig. 4. Schematic of the storage tank test rig.

Table 3
Measurement instruments.

Measured parameters	Devices	Measuring range	Accuracy
Temperature	K-type thermocouples	0–1100 °C	±0.75%t/°C
Inlet/outlet pressure	MIK-P300 Gage pressure transducer	0–0.6 MPa	±0.5% FS
Air flow rate	LUGB vortex flowmeter	0-600 Nm^3/h	±1.5% FS

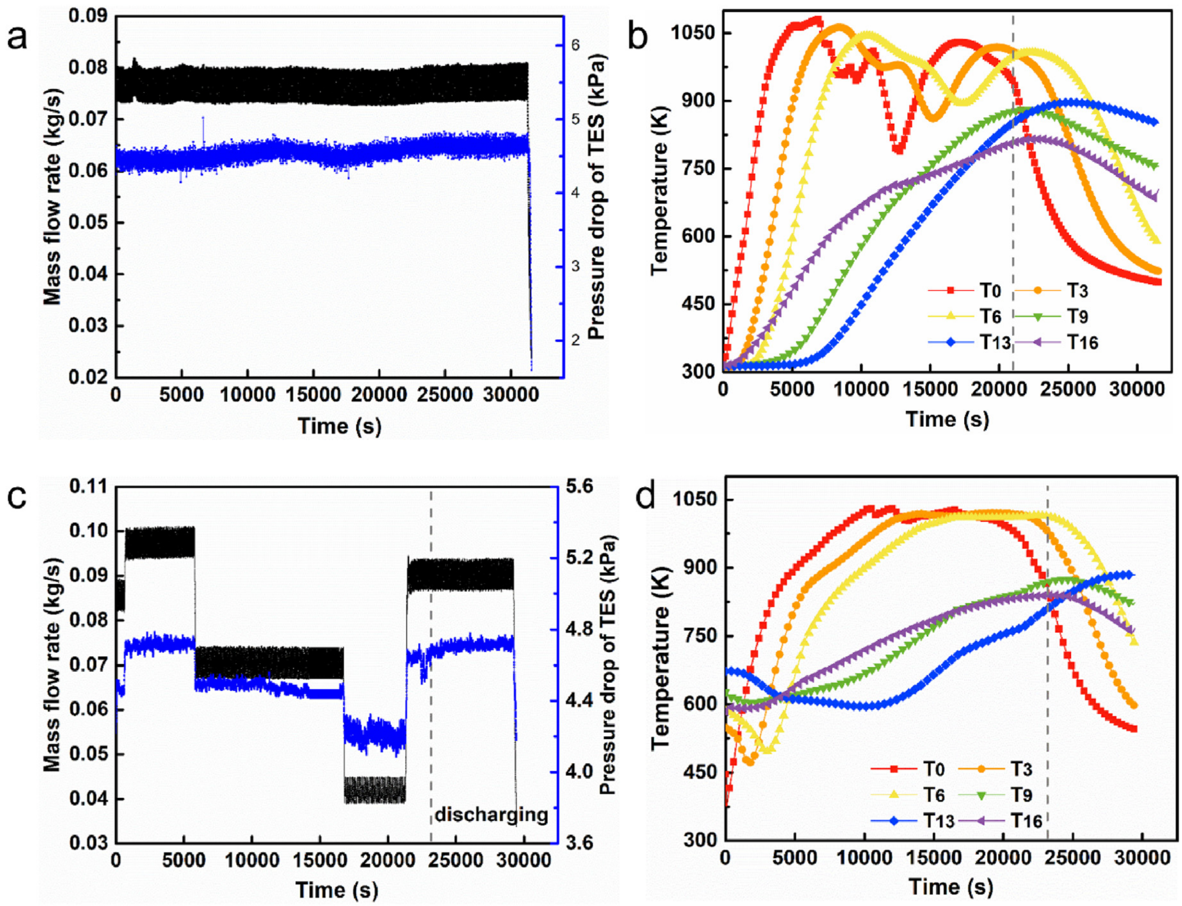

Fig. 5. Temperature changes with the operating time: (a) the temperatures of receiver and TES in the first test, (b) the temperatures at different layers in the first test, (c) the temperatures of receiver and TES in the second test, and (d) the temperatures at different layers in the second test.

latter layers by the flowing air. It should be noted that the quickly increase of the outlet air temperature T_{16} might be attributed to the air leakage from the gaps of the front modules, that is, a small amount of hot air leaked from the front layers and mixed with the cold air at the outlet of the modules. And the lower peak temperature of the 9th layer compared with the 13th layer could be attributed to the heat loss near the main hole due to the insufficient thermal insulation.

As shown in Fig. 5d, temperature profiles of the modules were very similar with that in the first test. All the module layers were firstly cooled down since the inlet air temperature T_0 was lower than the temperature of the modules. Overall, the temperatures of the front layers showed more rapid and dramatic changes than those of the latter layers. This was probably caused by the decrease of air flow rate in the latter layers due to the leakage problem, which led to the less heat amount transferred between the air and the modules. Due to the short discharging period, the temperature of 13th layer didn't show a drop.

4.3. Model development

The transient TES model is a one-dimensional discretized lumped-volume model [28]. As illustrated in Fig. 6a, both the fluid zone and the solid zone are discretized into M cells in the flow direction and each cell is considered as a lumped-volume. The thermal energy conservation differential equations of all the cells are solved for every moment. For model simplification, the temperature distribution on each module layer is considered to be uniform, i.e., the heat conduction perpendicular to flow direction can be neglected. The flow distribution on the cross section of storage tank is also assumed to be uniform with the deflector arranged at the inlet and the outer insulation layer is adiabatic.

Considering the leaking effects on the TES performance. The model is further modified by adding a leakage ratio α to calculate the mass flow rate of air through each module layer as defined in Eq. (11).

$$\alpha_i = \frac{\dot{m}_i}{\dot{m}} \tag{11}$$

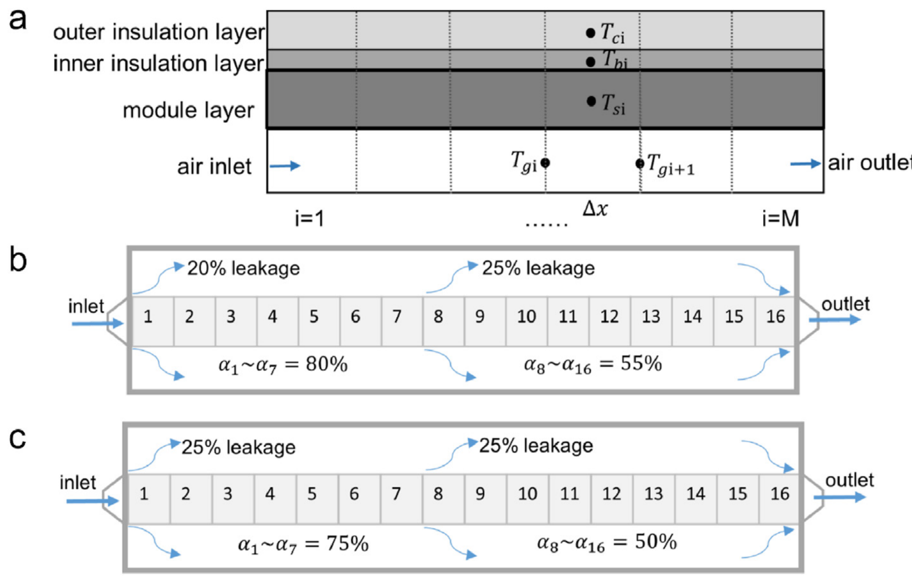

Fig. 6. (a)1D transient TES model, and schematic of air leakage in (b) the first test and (c) the second test.

Here the subscript i represents the layer position (1–16), $\dot{m}_i$ is the air mass flow rate through the corresponding layer, and $\dot{m}$ is the total air mass flow rate into the stacked modules.

As illustrated in Fig. 6b and c, the leakage ratios are 80% (α_1~α_7) and 55% (α_8~α_{16}) in the first test, and decreased to 75% (α_1~α_7) and 50% (α_8~α_{16}) in the second test. At the outlet of the stacked modules, all the leaked air mixes again with the rest of the air that flows through the modules. As no heat transfer is assumed between the modules and the leaked air, the specific enthalpy of the mixed air at the outlet h_{out} is equal to the mass-weighted average of the specific enthalpy of each part of the air h_i as shown in Eq. (12).

$$h_{out} = \sum_i \alpha_i h_i \tag{12}$$

Main structure parameters in the TES model and the physical properties of the insulation layers are listed in Table 4 and Table 5, respectively.

The flow state is basically laminar and the Nusselt number inside the module channels is calculated by Eq. (13) [17,20].

$$Nu = 3.66 + \frac{0.0668 Re \cdot Pr \cdot (d_h/L)}{1 + 0.04 (d_h/L \cdot Re \cdot Pr)^{2/3}} \tag{13}$$

The pressure drop was calculated by fitting test data as a function of mass flow rate without considering the influence of the inlet pressure and temperature as shown in Eq. (14).

Table 4
Main structure parameters of TES model.

Parameters	Value
Total mass of modules M_{st}	835 kg
Total cross-sectional area A_{sf}	0.49 m^2
Total length L_h	1.6 m
Hydraulic diameter of flow channel d_h	4 mm
Heat transfer area between air and modules A_h	350.54 m^2
Module cross-sectional area A_s	0.27 m^2
Flow cross-sectional area A_g	0.22 m^2
Outer diameter of inner insulation layer d_b	1.18 m
Cross-sectional area of inner insulation layer A_{sb}	0.31 m^2
Outer diameter of outer insulation layer d_c	1.53 m
Cross-sectional area of outer insulation layer A_{sc}	0.73 m^2

Table 5
Properties of the insulation layers.

Properties	castables	alumina-silicate fiber felt
Density ($kg \cdot m^{-3}$)	$\rho_b = 1200$	$\rho_c = 150$
Thermal conductivity ($W \cdot m^{-1} \cdot K^{-1}$)	$\lambda_b = 0.3$	$\lambda_c = 0.156$
Specific heat capacity ($J \cdot kg^{-1} \cdot K^{-1}$)	$c_{pb} = 1000$	$c_{pc} = 1000$

$$\Delta p = 6.38499 \dot{m}^{0.13152} \tag{14}$$

The thermal energy conservation differential equations for the fluid layer, the module layer, the inner insulation layer and the outer insulation layer in the unit length are calculated as shown in Eq. (15) – (18).

$$\frac{\partial(\rho_g A_g C_{vg} T_g)}{\partial t} = \frac{\partial(\dot{m} h_g)}{\partial x} - h \frac{A_h}{L_h}(T_g - T_s) \tag{15}$$

$$\frac{\partial(\rho_s A_s C_{ps} T_s)}{\partial t} = \lambda_s A_s \frac{\partial^2 T_s}{\partial x^2} + h \frac{A_h}{L_h}(T_g - T_s) - \frac{2\pi\lambda_b}{\ln(d_b/d_s)}(T_s - T_b) \tag{16}$$

$$\frac{\partial\left(\rho_b A_{sb} C_{pb} T_b\right)}{\partial t} = \lambda_b A_{sb} \frac{\partial^2 T_b}{\partial x^2} + \frac{2\pi\lambda_b}{\ln(d_b/d_s)}(T_s - T_b) - \frac{2\pi\lambda_c}{\ln(d_c/d_b)}(T_b - T_c) \tag{17}$$

$$\frac{\partial(\rho_c A_{sc} C_{pc} T_c)}{\partial t} = \lambda_c A_{sc} \frac{\partial^2 T_c}{\partial x^2} + \frac{2\pi\lambda_c}{\ln(d_c/d_b)}(T_b - T_c) \tag{18}$$

Here T_g、T_s、T_b、T_c are the temperatures of air, module, inner insulation layer and outer insulation layer, respectively. The unsteady term $\frac{\partial T}{\partial t}$ is discretized by the forward difference scheme. The diffusion term $\frac{\partial^2 T}{\partial x^2}$ is discretized by the implicit central difference scheme in the flow direction. The calculation time step Δt is 2s according to the data sampling frequency in the test. There are 16 module layers so the cell number M is 16 in the model.

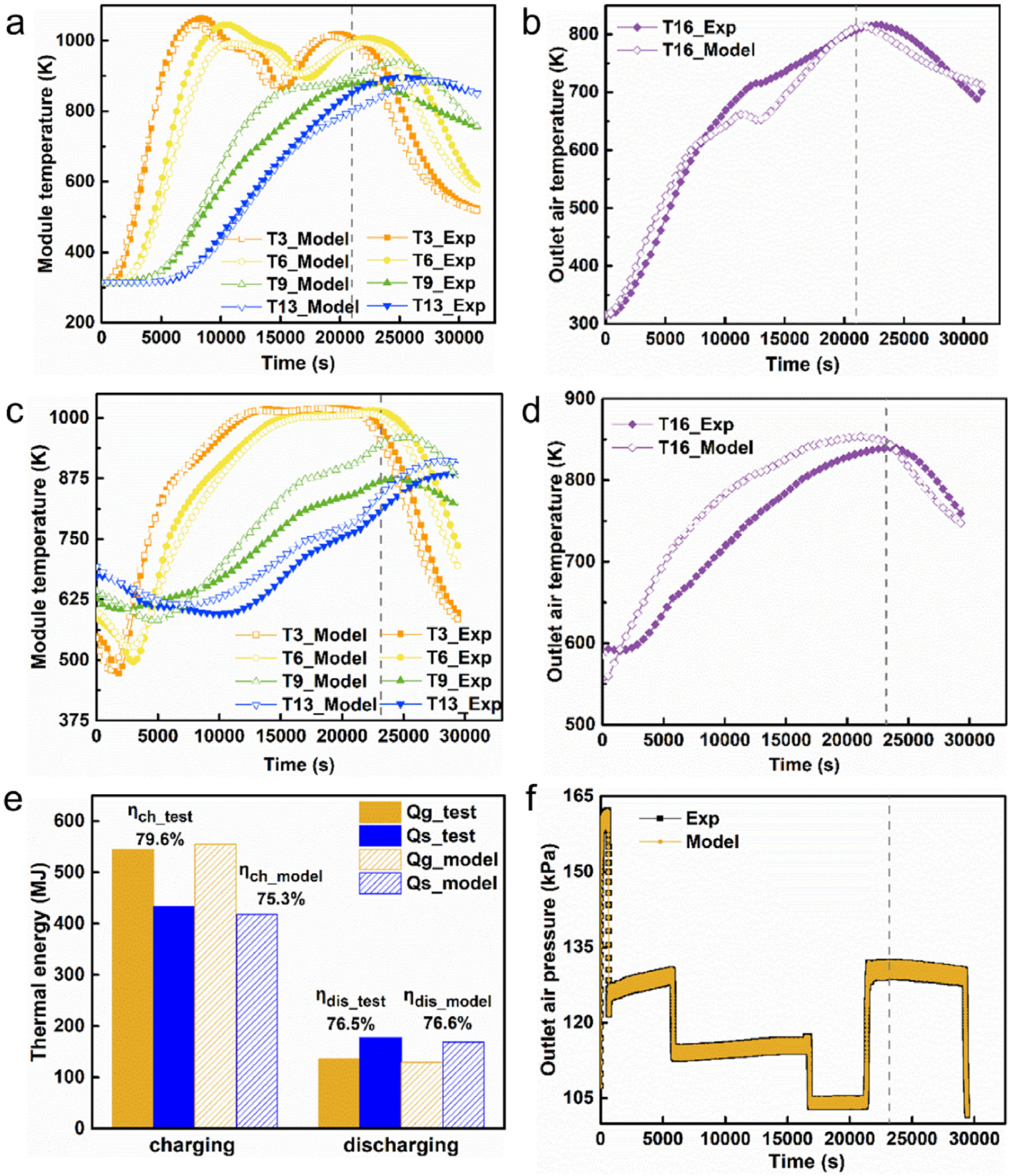

Fig. 7. Model validation by comparing the test results with simulation results: (a) the module temperature in the first test, (b) the outlet air temperature in the first test, (c) the module temperature in the second test, (d) the outlet air temperature in the second test, (e) the thermal energy and the thermal efficiency in the first test, (f) the outlet pressure in the second test.

The average thermal efficiency of the storage for the charging and discharging processes are defined as shown in Eqs. (19) and (20).

$$\eta_{ch} = \frac{Q_s}{Q_g} = \frac{\int_0^{L_h} M_s C_s (T_{st} - T_{s0}) dx}{\int_0^t \dot{m} C_p (T_{gin} - T_{gout}) dt} \tag{19}$$

$$\eta_{dis} = \frac{Q_g}{Q_s} = \frac{\int_0^t \dot{m} C_p (T_{gout} - T_{gin}) dt}{\int_0^{L_h} M_s C_s (T_{s0} - T_{st}) dx} \tag{20}$$

Here the subscripts *ch* and *dis* represent charging process and the discharging process and t is the charging/discharging duration. T_{s0}, T_{st}, T_{gin}, and T_{gout} are the initial, the final, the inlet and the outlet temperatures, respectively. Q_s and Q_g are the total thermal energy stored/released by the modules and the air.

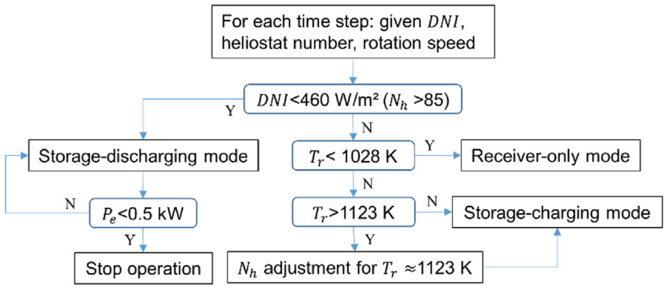

Fig. 8. Flow chart of the operation strategy.

N_h larger than 85. The receiver is bypassed to reduce the pressure drop and heat loss of the system in this mode. The system stops the operation when P_e is less than 0.5 kW. Fig. 9 illustrates both the system operation diagrams in storage-charging mode and storage-discharging mode.

As shown in Fig. 10a, a practical measured *DNI* during a day (7:30–16:00) was used in the calculation. The initial module temperature in the TES was assumed to be 653 K while the receiver and the recuperator were heated from ambient temperature (303 K). 60 heliostats were used in the receiver-only operation mode from 7:30–8:30, where the rotation speed reached the design value 120 krpm at 7:45 and the output electric power continuously

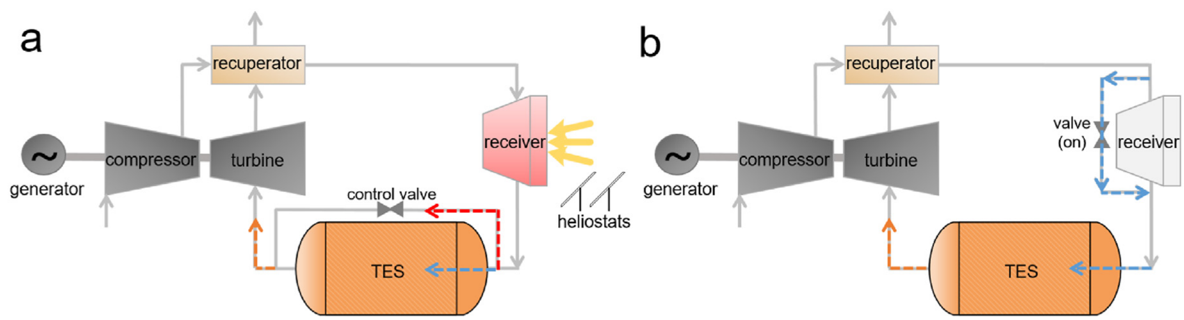

Fig. 9. System operation diagrams in (a)storage-charging mode, (b)storage-discharging mode.

For model validation, the calculation results and the test results of the module temperature, the outlet air temperature, the outlet pressure, the thermal energy and the thermal efficiency were compared as shown in Fig. 7. The relative root mean square errors of the module temperature and the outlet air temperature were below 4.76% and 2.82% for the first test, and 2.81% and 3.02% for the second test. The outlet pressures were also compared between the test and simulation results, where the relative root mean square error was below 0.2%. The relative errors of thermal energy (Q_s, Q_g) and thermal efficiency (η_{ch}, η_{dis}) are all within 5.5% for the first test.

5. Operation performance prediction of system

To verify the feasibility of the thermal storage tank, a transient system model is established to simulate the system operation during a typical day. The thermodynamic equilibrium state parameters of each component at different moments were calculated with a time step of 30 s. Other component models, including performance maps of the compressor and the turbine, the transient recuperator model and the transient receiver model, are developed and used in the system model.

Fig. 8 shows an operation strategy of constant output electric power (~12 kW) with constant rotation speed (120 krpm) and constant *TIT* (1028 K). In operation, the maximum receiver outlet temperature is controlled at 1123 K by adjusting the number of heliostats N_h (<85) to avoid overheating and the heliostat field efficiency is assumed to be constant. The receiver outlet temperature T_r and the *DNI* are the key criteria in switching the system modes among the receiver-only mode, the storage-charging mode, and the storage-discharging mode. With low *DNI* at the beginning of the operation, the system works in the receiver-only mode until T_r reaches 1028 K and the output power P_e reaches 12 kW, after which the TES is charged and the opening of the control valve is adjusted to keep P_e around 12 kW (*TIT* around 1028 K) in the storage-charging mode. Finally, the storage-discharging mode begins when the *DNI* declines below the threshold (460 W/m^2) with

increased to 11.88 kW with the outlet temperature of the receiver reaching 1028 K (Fig. 10b–d). The system began to generate electric power at 705 K of the *TIT* at 7:50 (Fig. 10d). The storage-charging operation lasted from 8:30 to 16:00. With the outlet temperature of the TES rising, the mass flow rate through the TES gradually increased by reducing the opening of control valve in order to keep the constant output power (Fig. 10c–e). With the *DNI* approaching its peak (780 W/m^2), the number of heliostats was reduced to the minimum 50 to avoid overheating of the receiver, after which it started to increase to make up the decrease of *DNI* and maintain a high receiver outlet temperature of 1123 K (Fig. 10a and c). At the end of charging period, all the modules in the TES reached above 940 K (Fig. 10f). The calculated amount of thermal energy stored in the TES was about 338.9 MJ with an average thermal efficiency of 75.43%. Main operation results of this solar thermal power system without the TES were also simulated as shown in Fig. 10c and d. The heliostat number was 48 in order to keep the maximum receiver outlet temperature at around 1123 K. Both the *TIT* and output electric power changed with *DNI* for the system without a TES. The system generated more output power than 12 kW during 9:36–15:06 with *DNI* higher than 620 W/m^2 and the *TIT* above 1208 K. By integrating the TES, *TIT* could be lower down by charging the TES with partial high-temperature air, that is, excessive heat absorbed by air was stored in the TES, which could extend the power generation duration for the system.

In the discharging period, the system switched to the storage-discharging mode with a constant rotation speed (114 krpm, 95% of the design value) to ensure a >12% surge margin at different operating points and a 3-h discharging period as shown in Fig. 10e and d. At the beginning of the discharging process, there was an obvious increase in power generation efficiency of the system without utilizing the receiver who had a comparatively low thermal efficiency. With the decrease of *TIT*, the output electric power also decreased (Fig. 10d) with the working point of the compressor moving away from the surge condition (Fig. 10e). At the end of the discharging period (19:08), the outlet temperature of the storage

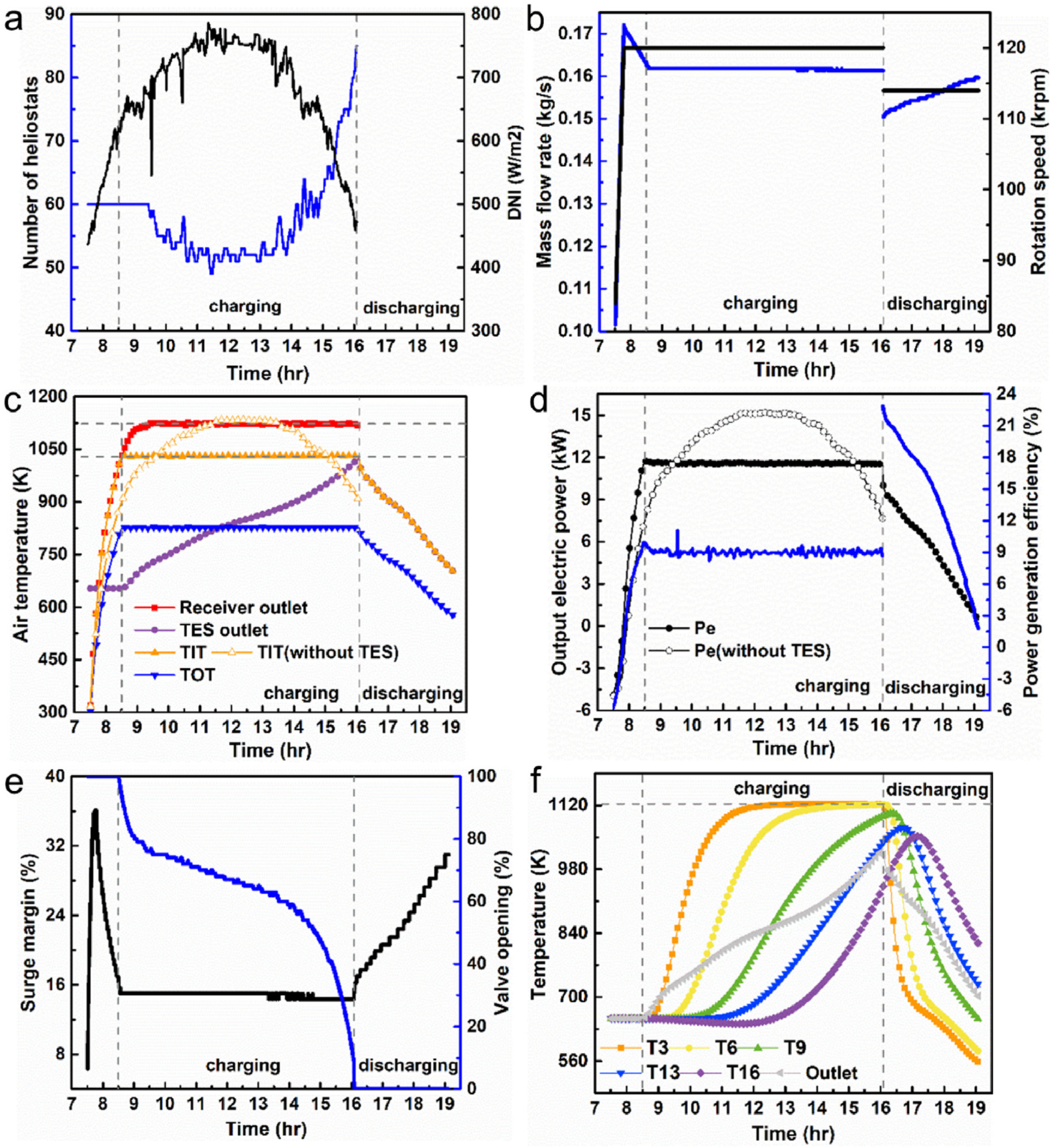

Fig. 10. Main results of the system operation.

tank decreases to 697 K (Fig. 10f) and the average thermal efficiency of the TES in discharging process was 90.97%. The discharging period lasted for 3 h, during which the average output power and efficiency were increased to 5.42 kW and 14.96%, respectively. In general, the TES designed in this paper could meet the requirements for the system operation during the discharging process.

6. Conclusion

A thermal energy storage (TES) tank was designed in this paper feasible for the application in solar thermal air-Brayton cycles. Both experimental tests and mathematical simulations were conducted for the performance analysis. An operation strategy of the system was further proposed and simulated using a transient model.

Air leakage was found to affect the temperature responses of module layers in the TES, where the front module layers were found to presented similar trends with the temperature change of inlet air, while the later layers showed relative steady changes. The thermal efficiency of the TES in charging process and discharging process could reach 79% and 76% during the tests. One-dimensional transient TES model was further built with the consideration of air leakage effects, where high accuracies were obtained in the predictions of module temperature (relative root mean square error of 4.76%), the outlet air temperature (relative root mean square error of 3.02%), the outlet pressures (relative root mean square error of 0.2%), and thermal energy/efficiency (relative error of 5.5%).

Overall, the simulation results of system operating process during a day showed that the integrated TES-solar air-Brayton cycle system could realize constant output electric power (~12 kW) during its storage-charging operation period. Besides, the designed TES could extend the power generation duration for 3 h with an average output electric power of 5.42 kW without solar radiation.

The small-scale solar thermal air-Brayton cycle power system, as a competitive distributed power system, is a promising solution to provide electricity access in some remote rural areas with abundant solar energy resource but scarce water supplies, such as sub-Saharan Africa [34,35]. With low-cost thermal energy storage, stable electricity output and extended power supply duration could be expected. Besides, this system achieves zero carbon emissions, which has a great potential for development under the background of global emission reduction.

Further improvements will focus on performance optimization of solar air receiver for high energy conversion efficiency of the system. What's more, thermochemical energy storage device with higher energy density, good chemical stability and good heat transfer performance will also be studied.

Credit author statement

Xin Zhou: Methodology, Software, Validation, Formal analysis, Investigation, Writing – original draft. Haoran Xu: Writing – original draft, Writing – review & editing. Duo Xiang: Methodology, Validation, Investigation. Jinli Chen: Methodology, Validation, Investigation, Formal analysis. Gang Xiao: Conceptualization, Writing – review & editing, Supervision, Project administration, Funding acquisition.

Declaration of competing interest

The authors declare that they have no known competing financial interests or personal relationships that could have appeared to influence the work reported in this paper.

Acknowledgment

The authors gratefully acknowledge the support from the Zhejiang Provincial Natural Science Foundation (NO. LR20E060001) and the National Natural Science Foundation of China (No.51776186). The authors also acknowledge the support from partners in SolGATS project (Concentrated solar power micro gas turbine with thermal energy storage) – City, University of London and Samad Power Ltd (UK).

Appendix A. Component models and validation

A.1 Compressor and turbine

A centrifugal compressor and a radial turbine are detailed designed according to the system design condition. As is shown in Fig. A.1 and Fig. A.2, performance maps of the centrifugal compressor and the radial turbine are used as their models in this paper, which are obtained by numerical simulation using ANSYS-CFX solver.

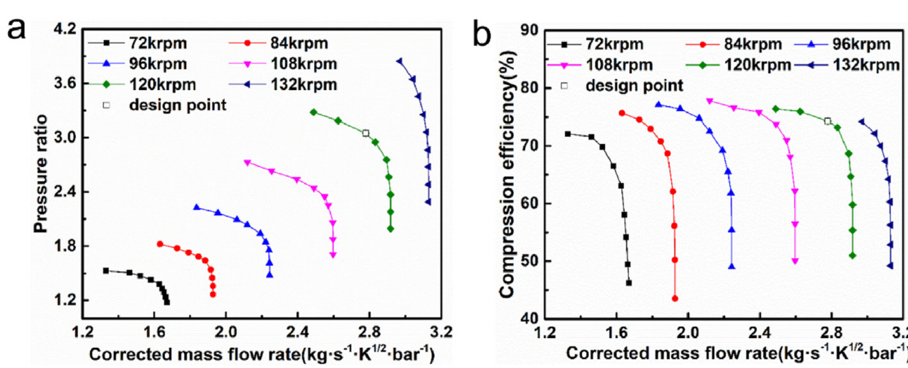

Fig. A.1. Centrifugal compressor performance map (a) corrected mass flow rate vs pressure ratio, (b) corrected mass flow rate vs adiabatic compression efficiency.

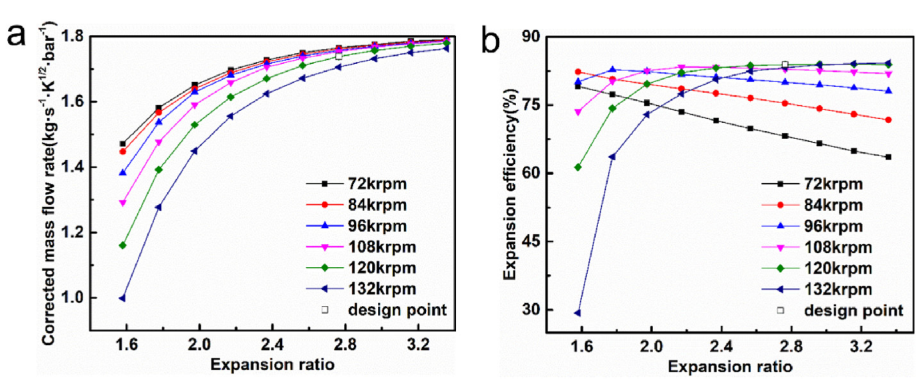

Fig. A.2. Radial turbine performance map (a) expansion ratio vs corrected mass flow rate, (b) expansion ratio vs adiabatic expansion efficiency.

For the compressor, total-to-total pressure ratio π_c is defined by Eq. (A.1).

$$\pi_c = p_{o1}/p_{o0} \tag{A.1}$$

Here p_{o1} and p_{o0} are total pressure at compressor outlet and inlet, respectively.

The total-to-total compression efficiency is the ratio of ideal input power in isentropic compression process $\dot{W}_{cs}$ and actual input power $\dot{W}_c$ as shown in Eq. (A.2).

$$\eta_c = \frac{\dot{W}_{cs}}{\dot{W}_c} = \frac{h_{o1s} - \mathrm{h}_{o0}}{h_{o1} - \mathrm{h}_{o0}} \tag{A.2}$$

Here h_{o1} and h_{o1s} are stagnation specific enthalpy at compressor outlet in actual compression process and isentropic compression process, respectively. h_{o0} is the stagnation specific enthalpy at compressor inlet.

For one given rotation speed and mass flow rate, the pressure ratio and compression efficiency can be obtained from the map. Since fluid velocity at the compressor outlet is small, the outlet static temperature is calculated by Eq. (A.3).

$$\frac{T_1}{T_0} \approx \frac{T_{o1}}{T_{o0}} = \frac{1}{\eta_c}\left(\pi_c^{\frac{\gamma-1}{\gamma}} - 1\right) + 1 \tag{A.3}$$

Here T_1 and T_{o1} are static temperature and total temperature at compressor outlet, respectively. T_0 and T_{o0} are static temperature and total temperature at compressor inlet, respectively.

It can be seen from the Fig. A.1a that the compressor works stably within a certain mass flow rate range at a rotation speed. The smaller mass flow rate than the minimum value leads to the surge condition where the compressor can't operate normally. Surge margin (*SM*) is usually defined to indicate the degree to which the working point is away from the surge point at a certain rotation speed as shown in Eq. (A.4). According to the experience of researchers, *SM* should be larger than 10%–12% during the operation [26,27].

$$SM = \frac{\dot{m}/\pi_c}{(\dot{m}/\pi_c)_s} - 1 \tag{A.4}$$

Here $\dot{m}/\pi_c$ is the ratio of mass flow rate and pressure ratio. The numerator is the ratio of the working point and the denominator is the ratio of the surge point. For the design point of compressor, *SM* is about 20.36%.

For the turbine, total-to-static expansion ratio π_t and total-to-static expansion efficiency η_t are used as shown in Eqs. (A.5) – (A.6).

$$\pi_t = p_{o2}/p_3 \tag{A.5}$$

$$\eta_t = \frac{\dot{W}_t}{\dot{W}_{ts}} = \frac{h_{o2} - h_3}{h_{o2} - h_{3s}} \tag{A.6}$$

Here p_{o2} and p_3 are total pressure at turbine inlet and static pressure at turbine outlet, respectively. h_3 and h_{3s} are static specific enthalpy at turbine outlet in actual expansion process and isentropic expansion process, respectively. $\dot{W}_t$ and $\dot{W}_{ts}$ are turbine output power in actual expansion process and isentropic expansion process, respectively.

For one given rotation speed and expansion ratio, the outlet static temperature T_3 is calculated by Eq. (A.7).

$$\frac{T_3}{T_2} \approx \frac{T_3}{T_{o2}} = 1 - \eta_t\left(1 - \pi_t^{\frac{1-\gamma}{\gamma}}\right) \tag{A.7}$$

Here T_{o2} and T_2 are total temperature and static temperature at turbine inlet, respectively.

A.2 Recuperator

The recuperator is developed by City, University of London for SolGATS (Concentrated Solar Power micro gas turbine with thermal energy storage) project [31]. Primary-surface structure is adopted because of the larger heat transfer area, less volume and weight. The cold flow channels and hot flow channels are alternately arranged and separated by metal plates. The transient recuperator model is shown in Fig. A.3, which is simplified as a hot fluid layer, a cold fluid layer, a metal plate layer and an insulation layer. Each layer is discretized into *M* cells in the flow direction. The thermal energy conservation differential equations for the recuperator in the unit length are calculated as shown in Eq. (A.8) – (A.11).

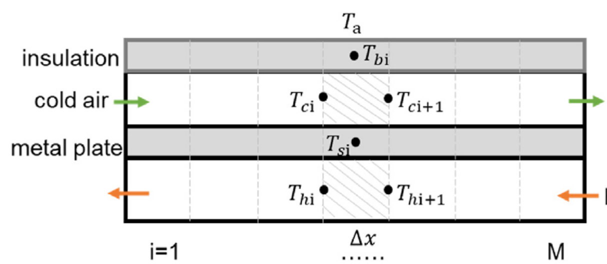

Fig. A.3. 1D transient recuperator model.

$$\frac{\partial\left(\rho_h A_{gh} C_{vh} T_h\right)}{\partial t} = \frac{\partial\left(\dot{m} h_f\right)}{\partial x} - h_h\frac{A_{hh}}{L}(T_h - T_s) \tag{A.8}$$

$$\frac{\partial(\rho_c A_{gc} C_{vc} T_c)}{\partial t} = \frac{\partial\left(\dot{m} h_f\right)}{\partial x} + h_c\frac{A_{hc}}{L}(T_s - T_c) - h_c\frac{A_{hb}}{L}(T_c - T_b) \tag{A.9}$$

$$\frac{\partial(\rho_s A_s C_{ps} T_s)}{\partial t} = \lambda_s A_s\frac{\partial^2 T_s}{\partial x^2} + h_h\frac{A_{hh}}{L}(T_h - T_s) - h_c\frac{A_{hc}}{L}(T_s - T_c) \tag{A.10}$$

$$\frac{\partial\left(\rho_b A_b C_{pb} T_b\right)}{\partial t} = \lambda_b A_b\frac{\partial^2 T_s}{\partial x^2} + h_c\frac{A_{hb}}{L}(T_c - T_b) - h_a\frac{A_a}{L}(T_b - T_a) \tag{A.11}$$

Here T_h、T_c、T_s、T_b、T_a are the temperature of hot fluid, cold fluid, mental plate, insulation and the environment, respectively. h_f is specific enthalpy of the fluid, A_g is total cross-sectional area of flow channels, A_h is heat transfer area between air and metal plates, A_s is cross-sectional area of single metal plate,t_s is the thickness of a single metal plate, A_b is cross-sectional area of insulation layer,L is flow channel length, A_a is external surface area of insulation layer.

The effectiveness of recuperator ε is defined by Eq. (A.12).

$$\varepsilon = \frac{T_{cout} - T_{cin}}{T_{hin} - T_{cin}} \tag{A.12}$$

Here the subscripts *in* and *out* represent the inlet and outlet of channels, respectively.

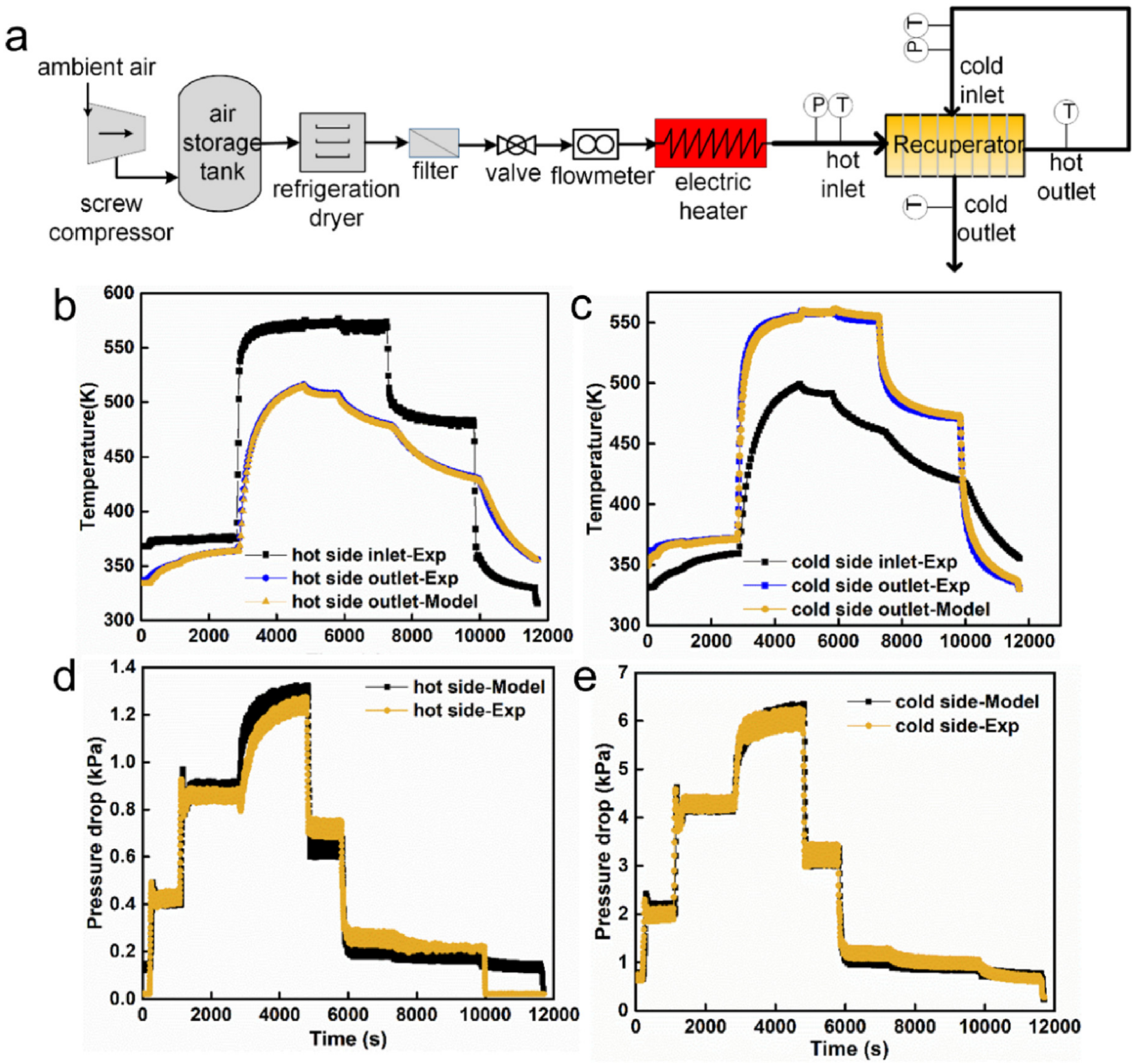

Fig. A.4. Validation of the recuperator model.

The recuperator was tested as shown in Fig. A.4a. The mass flow rate of air and inlet temperature of hot side were adjusted during the test. The outlet temperature and pressure drop of two sides were measured. Fig. A.4b and Fig. A.4c indicated that the outlet temperature of two sides calculated by the model agreed well with the test results. The relative root mean square error of outlet air temperature for two sides was below 0.71%. In terms of the outlet pressure, the maximum relative error of two sides was 0.25%.

Based on test data, pressure drop calculation formulas of both the hot side and cold side were fitted as Eqs. (A.13) – (A.14).

$$\Delta P_h = 0.06602\overline{T}_{in} \cdot \dot{m}^{1.719355} \tag{A.13}$$

$$\Delta P_c = 0.254565\overline{T}_{in} \cdot \dot{m}^{1.632355} \tag{A.14}$$

Here $\overline{T}_{in}$ is the average value of the inlet temperature at two sides. Fig. A.4e showed that there was large discrepancy between the measured and the calculated hot side pressure drop under small mass flow rate condition (<0.05 kg/s), where the fitting formula was inapplicable.

A.3 Receiver

The solar collector system consists of an air receiver, a solar tower and a heliostat field. Fig. A.5a demonstrates the solar tower and heliostat field that are constructed at the research center of Zhejiang University [32]. There are 100 heliostats in the field. The tubular air receiver designed by Xiao et al. [33] is shown in Fig. A.5b.

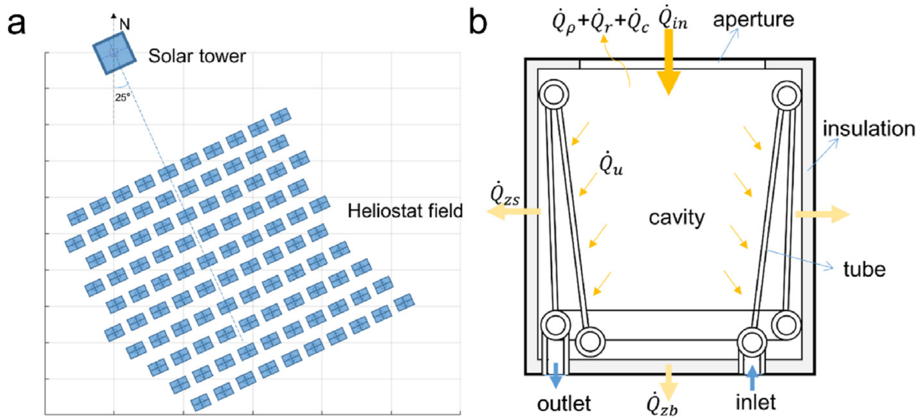

Fig. A.5. Schematic of solar collector system.

The transient receiver model is based on the energy conservation equation by reference to the study of Chen et al. [8,32,33]. As can be seen in Fig. A.5b, total incident radiation power is $\dot{q}_{in}$, part of which $\dot{q}_\rho$ is reflected by the receiver cavity and finally overflows from the aperture. There are radiation heat loss $\dot{q}_r$ and natural convection heat loss $\dot{q}_c$ between the high-temperature tube walls and the environment. The conduction heat loss through the insulation is $\dot{q}_{zs}$ and $\dot{q}_{zb}$. Thermal power absorbed by air is $\dot{q}_u$. Therefore, the energy conservation equation of the receiver is described by Eq. (A.15).

$$\dot{q}_u = \dot{q}_{in} - (\dot{q}_\rho + \dot{q}_r + \dot{q}_c + \dot{q}_{zs} + \dot{q}_{zb}) = \dot{m}c_p(T_{out} - T_{in}) \tag{A.15}$$

$$\eta_{receiver} = \dot{q}_u / \dot{q}_{in} \tag{A.16}$$

Here the calculation formula of each heat loss term is derived from the work carried out by Xiao et al. [33]. Incident radiation power $\dot{q}_{in}$ is related to the direct normal irradiance *DNI*, total reflective area of the field A_{field}, the efficiency of the field η_{field} and the intercept factor of receiver η_{inter} as shown in Eq. (A.17).

$$\dot{q}_{in} = DNI \cdot A_{field} \cdot \eta_{field} \cdot \eta_{inter} \tag{A.17}$$

As is seen in Fig. A.6, the receiver model is simplified as the front tube layer (the half tube surface receiving the radiation heat), air layer, the back tube layer (the other half tube surface) and the insulation layer. The thermal energy conservation differential equations for the recuperator in the unit length are calculated as shown in Eq. (A.18) – (A.21).

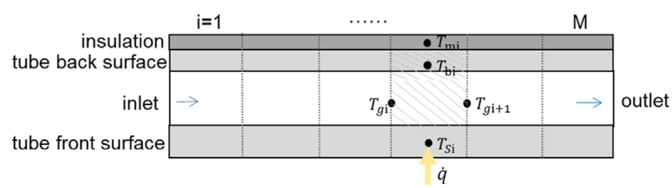

Fig. A.6. 1D transient receiver model.

$$\frac{\partial(\rho_s A_s C_{ps} T_s)}{\partial t} = \lambda_s A_s \frac{\partial^2 T_s}{\partial x^2} - h\frac{A_h}{L}(T_g - T_s) - \frac{\lambda_s N_t t_t}{\frac{\pi(D_t - t_t)}{2}}(T_s - T_b) + \dot{q} \tag{A.18}$$

$$\frac{\partial(\rho_g A_g C_{vg} T_g)}{\partial t} = \frac{\partial(\dot{m} h_f)}{\partial x} + h\frac{A_h}{L}[(T_g - T_s) - (T_g - T_b)] \tag{A.19}$$

$$\frac{\partial(\rho_s A_s C_{ps} T_b)}{\partial t} = \lambda_s A_s \frac{\partial^2 T_b}{\partial x^2} + h\frac{A_h}{L}(T_g - T_b) + \frac{\lambda_s N_t t_t}{\frac{\pi(D_t - t_t)}{2}}(T_s - T_b) \tag{A.20}$$

$$\frac{\partial(\rho_m A_m C_{pm} T_m)}{\partial t} = \lambda_m A_m \frac{\partial^2 T_m}{\partial x^2} + \frac{2\pi\lambda_m}{\ln(D_{eisol}/D_{iisol})}(T_b - T_m) - h_a\frac{A_a}{L}(T_m - T_a) \tag{A.21}$$

Here T_s、T_g、T_b、T_m、T_a are the temperature of front tube layer, air layer, back tube layer, insulation and the environment, respectively. N_t is number of tubes, D_t is inner diameter of tube, t_t is wall thickness of tube, D_{iisol} and D_{eisol} are inner and outer diameters of insulation layer, $\dot{q}$ is the incident radiation power of the tubes.

The outdoor test results of the air receiver were used to validate the model. The heating stage (2.25 h) and cooling stage (2.87 h) was simulated and compared with the test results in Fig. A.7. The efficiency of heliostat field was estimated to be 0.6 and the intercept factor of receiver was about 0.4. The relative root mean square error of the outlet air temperature was below 4.26%. Pressure drop calculation formula was also fitted by test data. The relative error of outlet pressure was within 0.15% (1.3 kPa) for both the heating and cooling stages.

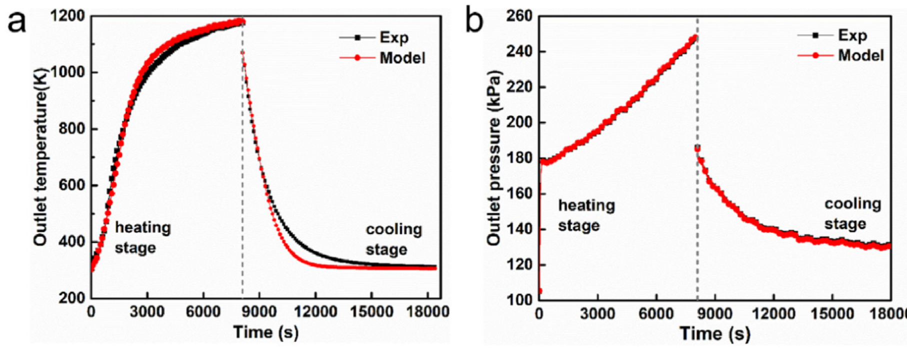

Fig. A.7. Validation of the receiver model.

Appendix B. Honeycomb ceramic module

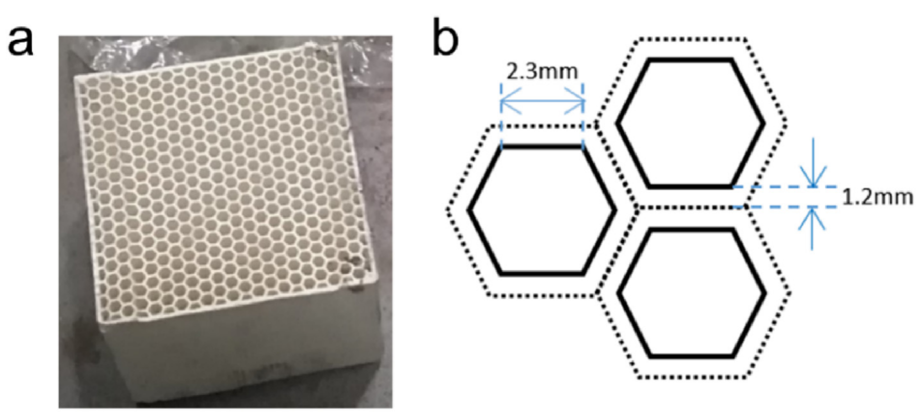

Fig. B.1. Honeycomb ceramic module (a) module photo, (b) honeycomb structure.

References

[1] Behar O, Khellaf A, Mohammedi K. A review of studies on central receiver solar thermal power plants. Renew Sustain Energy Rev 2013;23:12–39. https://doi.org/10.1016/j.rser.2013.02.017.

[2] Liu C. Summary of gas turbine power generation technology based on solar power. IOP Conf Ser Earth Environ Sci 2019;300:42050. https://doi.org/10.1088/1755-1315/300/4/042050.

[3] Mills D. Advances in solar thermal electricity technology. Sol Energy 2004;76: 19–31. https://doi.org/10.1016/S0038-092X(03)00102-6.

[4] Commonwealth Scientific Industrial Research Organization. Solar air turbine project final report: project results. 2014.

[5] Dickey B. Test results from a concentrated solar microturbine Brayton cycle integration. In: ASME turbo expo: turbine technical conference & exposition. ASME; 2011. p. 1031–6. https://doi.org/10.1115/GT2011-45918.

[6] Lanchi M, Montecchi M, Crescenzi T, Mele D, Miliozzi A, Russo V, et al. Investigation into the coupling of micro gas turbines with CSP technology: OMSoP project. Energy Procedia 2015;69:1317–26. https://doi.org/10.1016/j.egypro.2015.03.146.

[7] Aichmayer L, Garrido J, Laumert B. Thermo-mechanical solar receiver design and validation for a micro gas-turbine based solar dish system. Energy 2020;196:116929. https://doi.org/10.1016/j.energy.2020.116929.

[8] Chen JL, Xiao G, Ferrari ML, Yang TF, Ni MJ, Cen KF. Dynamic simulation of a solar-hybrid microturbine system with experimental validation of main parts. Renew Energy 2020;154:187–200. https://doi.org/10.1016/j.renene.2019.11.022.

[9] Barberis S, Traverso AN, Traverso A, Massardo AF. High temperature storage for CSP hybrid gas turbine: test rig dynamic analysis and experimental validation. Proceedings of ASME Turbo Expo 2016:1–11. https://doi.org/10.1115/GT2016-56202. 2016: turbomachinery technical conference and exposition.

[10] Stekli J, Irwin L, Pitchumani R. Technical challenges and opportunities for concentrating solar power with thermal energy storage. J Therm Sci Eng Appl 2013;5:21011. https://doi.org/10.1115/1.4024143.

[11] Cabeza LF. Advances in thermal energy storage systems. second ed. Cambridge: Woodhead Publishing; 2020.

[12] Wang Y, Bai FW, Wang ZF, Kiriki H, Han MX, Kubo S. Experimental research of the heat transfer characteristics using a packed-bed of honeycomb ceramic for high temperature thermal storage system. Energy Procedia 2015;69: 1059–67. https://doi.org/10.1016/j.egypro.2015.03.209.

[13] Selimovic F, Bruun T, Sundén B. Computational analysis of gas flow and heat transport phenomena in monolithic structures for high temperature processes. In: ASME 2005 summer heat transfer conference. ASME; 2005. p. 87–96.

[14] Zunft S, Hänel M, Krüger M, Dreißigacker V, Göhring F, Wahl E. Jülich solar power tower—experimental evaluation of the storage subsystem and performance calculation. J Sol Energy Eng 2011;133:031019. https://doi.org/10.1115/1.4004358.

[15] Zunft S, Hänel M, Krüger M, Dreißigacker V. A design study for regenerator-type heat storage in solar tower plants—results and conclusions of the HOT-SPOT project. Energy Procedia 2014;49:1088–96. https://doi.org/10.1016/j.egypro.2014.03.118.

[16] Mahmood M, Traverso A, Traverso AN, Massardo AF, Marsano D, Cravero C. Thermal energy storage for CSP hybrid gas turbine systems: dynamic modelling and experimental validation. Appl Energy 2018;212:1240–51. https://doi.org/10.1016/j.apenergy.2017.12.130.

[17] Luo ZY, Wang C, Xiao G, Ni MJ, Cen KF. Simulation and experimental study on honeycomb-ceramic thermal energy storage for solar thermal systems. Appl Therm Eng 2014;73:622–8. https://doi.org/10.1016/j.applthermaleng.2014.07.053.

[18] Schmidt FW, Szego J. Transient response of solid sensible heat thermal storage units—single fluid. J Heat Tran 1976;98:471–7. https://doi.org/10.1115/1.3450578.

[19] Andreozzi A, Buonomo B, Manca O, Tamburrino S. Thermal energy storages analysis for high temperature in air solar systems. Appl Therm Eng 2014;71: 130–41. https://doi.org/10.1016/j.applthermaleng.2014.06.036.

[20] Li Q, Bai FW, Yang B, Wang Y, Xu L, Chang ZS, et al. Dynamic simulations of a honeycomb ceramic thermal energy storage in a solar thermal power plant using air as the heat transfer fluid. Appl Therm Eng 2017;129:636–45. https://doi.org/10.1016/j.applthermaleng.2017.10.063.

[21] Watson N, Janota MS. Turbocharging the internal combustion engine. first ed. London: Palgrave; 1982. https://doi.org/10.1007/978-1-349-04024-7.

[22] Dixon SL, Hall C. Fluid mechanics and thermodynamics of turbomachinery. seventh ed. Oxford: Butterworth-Heinemann; 2014. https://doi.org/10.1016/C2011-0-05059-7.

[23] Xiao G, Yang TF, Liu HL, Ni D, Ferrari ML, Li MC, et al. Recuperators for micro gas turbines: a review. Appl Energy 2017;197:83–99. https://doi.org/10.1016/j.apenergy.2017.03.095.

[24] Le Roux WG, Bello-Ochende T, Meyer JP. The efficiency of an open-cavity tubular solar receiver for a small-scale solar thermal Brayton cycle. Energy Convers Manag 2014;84:457–70. https://doi.org/10.1016/j.enconman.2014.04.048.

[25] Wang Y, Bai FW, Yang B, Wang ZF. Heat transfer behavior of a combined sensible-latent thermal energy storage system for high temperature applications. Energy Storage Science and Technology 2017;6:719–25.

[26] Traverso A. TRANSEO: a new simulation tool for transient analysis of innovative energy systems. Genoa: University of Genoa; 2004.

[27] Yuan C, Chen B, Chen Z. Technology of Micro gas turbine power generation. first ed. Beijing: CHINA MACHINE PRESS; 2012.

[28] Guan Z, Zhang Z, Jiao J. Physical properties of inorganic materials. second ed. Beijing: TSINGHUA UNIVERSITY PRESS; 2011.

[29] Qi X, Liu Y. Heat storage performance of a honeycomb ceramic monolith. Open Fuel Energy Sci J 2014;7:113–20. https://doi.org/10.2174/1876973X01407010113.

[30] Singh A, Tescari S, Lantin G, Agrafiotis C, Roeb M, Sattler C. Solar thermochemical heat storage via the Co3O4/CoO looping cycle: storage reactor modelling and experimental validation. Sol Energy 2017;144:453–65. https://doi.org/10.1016/j.solener.2017.01.052.

[31] Thermo-Fluids Research Centre. SolGATS: concentrated solar power micro gas turbine with thermal energy storage. 2021. accessed 25 May 2021, https://researchcentres.city.ac.uk/thermo-fluids/turbomachinery-research-group#unit=research-projects.

[32] Li HF. Numerical and experimental study of a tubular air receiver for solar tower. Zhejiang University; 2020.

[33] Xiao G, Chen JL, Yang TF, Ni MJ, Cen KF, Liu SJ. Experiment and simulation study of tubular solar air receiver using a solar dish. Acta Energiae Solaris Sin 2019;40:3355–63.

[34] Hajat A, et al. Efficiency of solar power units for small-scale businesses in a remote rural area, South Africa. Renew Energy 2009;34(12):2722–7.

[35] Fluri TP. The potential of concentrating solar power in South Africa. Energy Pol 2009;37(12):5075–80.